Respiratory Research

RESEARCH Open Access

Single-cell landscape of mouse lungs exposed to intermittent hypoxia

Pengdou Zheng[1,2†], Lingling Wang[1†], Xiaoyan Zhu[1], Zhenyu Mao[1], Fengqin Zhang[1], Guisha Zi[1], Lixiang Chen[1], Huiguo Liu[1*], Ling Zhou[1*] and Wei Liu[3*]

Abstract

Background Obstructive sleep apnea–hypopnea syndrome (OSAHS) is a prevalent respiratory disorder characterized by intermittent hypoxia (IH), which promotes pulmonary complications. However, the cellular and molecular mechanisms underlying IH-induced lung remodeling remain poorly understood.

Methods We performed comprehensive single-cell RNA sequencing (scRNA-seq) analysis of lung tissue from IH-exposed mice (GSE145435). Computational approaches were used to characterize cellular heterogeneity, transcriptional programs, and cell-cell interactions. Key findings were validated using intervention studies with the SP1 inhibitor plicamycin.

Results Our analysis revealed the following: IH induced: (1) the expansion of four distinct fibroblast subsets; (2) polarization of proinflammatory Mφ1 (IL-18 high) with activated PPAR signaling; (3) altered T-cell dynamics featuring $CD4^+$ T-cell accumulation and reduced memory T cells; (4) endothelial remodeling (endo2 subtype dominance) mediated by Ccl6–Ccr2 interactions. Moreover, SP1 inhibition attenuated IH-induced pathology, reducing collagen deposition and inflammatory markers.

Conclusions This study identifies SP1 as a master regulator of IH-induced pulmonary remodeling through coordinated control of fibrotic, inflammatory, and vascular pathways. These findings provide mechanistic insights into OSAHS-related complications and highlight SP1 inhibition as a potential therapeutic strategy for hypoxia-induced lung injury.

Keywords Intermittent hypoxia, Lung remodeling, Single-cell transcriptomics, SP1, OSAHS

Introduction

Obstructive sleep apnea–hypopnea syndrome (OSAHS) is a common sleep-related breathing disorder characterized by intermittent hypoxia (IH) and sleep fragmentation caused by airway stenosis or collapse during sleep [1]. According to epidemiological statistics, approximately 936 million people between the ages of 30 and 69 suffer from OSAHS worldwide. China has the largest number of OSAHS patients, with more than 176 million people, including 65.52 million with moderate to severe OSAHS [2]. According to a survey, the incidence of OSAHS increases with age, and the number of apnea

†Pengdou Zheng and Lingling Wang contributed equally to this work.

*Correspondence:
Huiguo Liu
huiguol@hust.edu.cn
Ling Zhou
471699217@tjh.tjmu.edu.cn
Wei Liu
404793938@tjh.tjmu.edu.cn

Full list of author information is available at the end of the article

© The Author(s) 2025. **Open Access** This article is licensed under a Creative Commons Attribution-NonCommercial-NoDerivatives 4.0 International License, which permits any non-commercial use, sharing, distribution and reproduction in any medium or format, as long as you give appropriate credit to the original author(s) and the source, provide a link to the Creative Commons licence, and indicate if you modified the licensed material. You do not have permission under this licence to share adapted material derived from this article or parts of it. The images or other third party material in this article are included in the article's Creative Commons licence, unless indicated otherwise in a credit line to the material. If material is not included in the article's Creative Commons licence and your intended use is not permitted by statutory regulation or exceeds the permitted use, you will need to obtain permission directly from the copyright holder. To view a copy of this licence, visit http://creativecommons.org/licenses/by-nc-nd/4.0/.

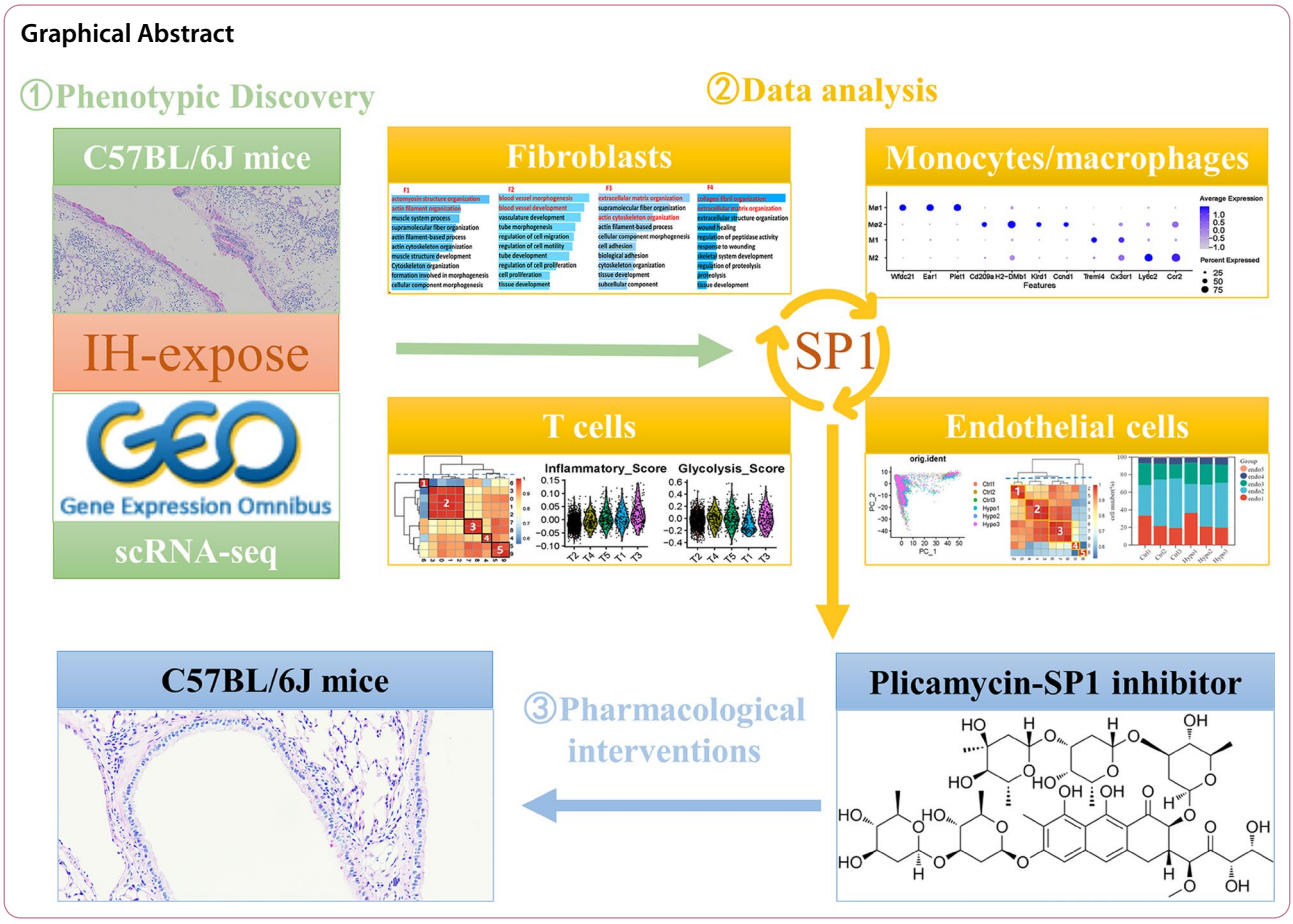

events occurring at night in healthy elderly individuals is usually higher than in middle-aged people, peaking after approximately age 65; these events are more common in men [3]. Over recent decades, understanding of OSAHS-related pathophysiology has progressed relatively slowly due to limitations in obtaining disease samples and developing disease models. However, many studies have confirmed the negative effects of OSAHS on various organs and systems throughout the body. Numerous observational studies have shown that OSAHS is associated with cardiovascular diseases and is a risk factor for hypertension, poor blood pressure control, stroke, myocardial infarction, heart failure, arrhythmia, sudden cardiac death, and all-cause mortality [4, 5]. In the liver, IH has been shown to cause insulin resistance, dysfunction of key steps in lipid metabolism, atherosclerosis, mitochondrial dysfunction, inflammation, and liver steatosis and fibrosis [6, 7]. Substantial changes in the gut microbiota have also been observed in both animal models of IH and samples from humans with OSAHS [8, 9]. In addition, recent studies have explored associations between IH and neurotoxicity, cancer progression, kidney dysfunction, and reproductive abnormalities [10–12].

The organ most directly affected by IH is the lungs. Despite advances in understanding the pathology of IH in various types of lung disease and dysfunction, the cellular characteristics of lungs exposed to IH remain largely unknown and obscure. While more research has focused on changes in the function of individual cells, the complex network of cell–cell interactions in the microenvironment has been largely neglected due to the difficulty of studying it[13].

The aim of this study was to establish a high-resolution single-cell landscape of different cell types by analyzing single-cell RNA sequencing (scRNA-seq) data from IH-exposed mouse lung tissue to fully understand the response of major cells in the lung to IH. The cellular and molecular features identified in this study not only enhance our understanding of the mechanisms driving chronic lung pathology in patients with OSAHS but also provide preliminary evidence supporting the therapeutic potential of targeting key regulatory factors, thereby informing future treatment strategies for OSAHS.

Materials and methods

Acquisition, dimensionality reduction and cellular annotation of scRNA-seq data

Six scRNA-seq datasets of mouse lung tissue were retrieved from the Gene Expression Omnibus (GEO, http://www.ncbi.nlm.nih.gov/geo/) database, specifically under accession number GSE145435 (details in Supplementary Table 1) [14]. These datasets were generated on the Illumina HiSeq 2500 platform, achieving a sequencing depth of 10 X coverage. Initial data processing was conducted using the Seurat package to ensure the selection of high-quality cells. The following quality control criteria were stringently applied: (1) each gene must be detected in a minimum of three cells; (2) a cell must exhibit at least 50 detected genes; (3) the mitochondrial gene content must not exceed 10% of the total detected genes; and (4) the number of transcripts per cell must range between 200 and 4000. Data normalization was performed using the log-normalization method, followed by the identification of 1,500 highly variable genes using the default 'vst' parameter, setting the stage for subsequent cell type classification [15]. Principal component analysis (PCA) was employed for initial linear dimensionality reduction, with the first 15 principal components (PCs) selected for further analysis [16]. Batch effects were mitigated using the Harmony algorithm, and the t-distributed stochastic neighbor embedding (t-SNE) algorithm facilitated clustering through nonlinear dimensionality reduction [17]. Marker genes for each cluster were identified using the FindAllMarkers function, with an adjusted P value threshold of < 0.05 and an absolute $\log_2$-fold change (FC) greater than 1 serving as selection criteria. Cell types were manually annotated for each cluster based on the expression of these marker genes. Finally, the Monocle algorithm was utilized to construct pseudotime trajectories, providing insights into the dynamic processes of cellular differentiation or gene expression patterns [18].

Animal models and therapeutic methods

Considering that OSAHS predominantly affects male patients, we used male C57BL/6J mice in this study. Male C57BL/6J mice aged 6–8 weeks were obtained from Wuhan SHULAIBAO Biotechnology Co., Ltd. All animals were housed under specific pathogen-free conditions with controlled temperature and humidity, a 12-hour light/dark cycle, and free access to sterilized chow and drinking water. All animal procedures were approved by the Animal Care and Use Committee of Tongji Hospital, Tongji Medical College, Huazhong University of Science and Technology. IH exposure was carried out using a programmable hypoxia chamber. Mice in the IH groups were exposed to IH for 8 h daily (from 8:00 a.m. to 4:00 p.m.) for 42 consecutive days. Each 4-minute cycle consisted of 150 s of hypoxia (5% O_2) followed by 90 s of normoxia (21% O_2), continuously repeated throughout the 8-hour exposure period [19, 20]. Control mice were maintained under normoxic room air conditions for the same duration. All mice were euthanized, and lung tissues were harvested 12 h after the final IH exposure on day 42.

Two independent experiments were conducted. In the first experiment, 12 mice were randomly divided into two groups ($n = 6$ per group): control and IH. In the second experiment, 24 mice were randomly assigned into four groups ($n = 6$ per group): control, IH, plicamycin, and IH + plicamycin. Plicamycin (HY-A0122, MCE), an SP1 inhibitor, was dissolved in a vehicle solution consisting of 10% DMSO, 40% PEG300, 5% Tween-80, and 45% saline, and administered intraperitoneally at a dose of 0.4 mg/kg in a final volume of 100 µL. Drug administration began on day 2 of IH exposure and was given every other day for a total of 21 injections. Each dose was administered approximately 30 min before the start of the daily IH session. In the IH + plicamycin group, mice were sacrificed 12 h after the final IH exposure and drug injection.

Histopathology analysis

After mice were anesthetized, lung tissues were fixed in 4% paraformaldehyde (PFA) at 4℃ for 24 h. After dehydration, the left lower lung was embedded in paraffin and cut into 4 µm-thick sections. Hematoxylin and eosin (H&E) staining was performed for pathological analysis. Peribronchial inflammation was semi-quantitatively scored by two blinded observers according to the following criteria: 0, no inflammatory cells; 1, a small number of inflammatory cells; 2, a single layer of inflammatory cells; 3, 2–4 layers of inflammatory cells; and 4, more than 4 layers of inflammatory cells surrounding the bronchi. For each section, three to five randomly selected, non-overlapping high-power fields were evaluated, and the mean score was calculated to represent the result for each animal. Periodic Acid–Schiff (PAS) staining, which detects polysaccharides such as glycogen and mucosubstances, was performed to assess goblet cell proliferation. PAS-positive (PAS+) goblet cells were counted in three to five randomly selected, non-overlapping high-power fields (HPFs, 400× magnification) per section, and the number of PAS + cells per 100 µm length in the airway was counted for each animal. Masson's staining was conducted to evaluate collagen deposition in the lungs. For each section, three to five randomly selected fields were analyzed, and collagen-positive areas were quantified using ImageJ software by calculating the percentage of blue-stained area relative to the total tissue area. The mean percentage across the selected fields was recorded as the result for each animal. Images were obtained using an optical microscope (Olympus/DP70, Tokyo, Japan).

Immunohistochemistry (IHC)

The paraffin-embedded sections of mouse lung tissue were dewaxed by sequential immersion in the following solutions: xylene I for 30 min, xylene II for 30 min, absolute ethanol I for 10 min, absolute ethanol II for 10 min, 95% ethanol for 5 min, 90% ethanol for 5 min, 80% ethanol for 5 min, 70% ethanol for 5 min, and finally rinsed in distilled water. Subsequently, the sections were placed in a container filled with EDTA antigen retrieval buffer (pH 8.0) and subjected to heat-induced epitope retrieval in a microwave oven. The antigen retrieval protocol involved heating at high power until the buffer boiled (approximately 3 min), then switching off the microwave and allowing the sections to incubate for 10 min at room temperature, followed by reheating at low power (simmer) for an additional 3 min. After natural cooling to room temperature, the sections were rinsed three times in phosphate-buffered saline (PBS, pH 7.4) on a shaker for 5 min each to remove residual buffer. After cooling to room temperature, the sections were incubated with 5% bovine serum albumin (BSA) for 30 min to block nonspecific antibody binding. Following blocking, the tissue sections were incubated overnight at 4℃ with primary antibodies against Cd11b (ab133357, 1:4000, Abcam), Mpo (ab208670, 1:1000, Abcam), CD68 (ab955, 1:3000, Abcam), and CD31 (ab28364, 1:40, Abcam). After primary antibody incubation, sections were washed three times with phosphate-buffered saline (PBS) to remove unbound antibodies. Subsequently, the sections were incubated with appropriate horseradish peroxidase (HRP)-conjugated secondary antibodies at room temperature for 1 h. After washing with PBS, antigen-antibody complexes were visualized using 3,3'-diaminobenzidine (DAB) chromogen, resulting in a brown precipitate at the antigen sites. The sections were then counterstained with hematoxylin for nuclear visualization. Following staining, sections were dehydrated through graded ethanol series (70%, 85%, 95%, and 100%), cleared in xylene, and mounted with a resinous mounting medium. Finally, stained sections were examined under a light microscope, and images were captured for analysis.

Immunofluorescence (IF) staining

The dewaxing, rehydration, and antigen retrieval steps were performed as described for immunohistochemistry (see IHC section above). Briefly, paraffin-embedded mouse lung tissue sections were dewaxed in xylene and rehydrated through a graded ethanol series, followed by antigen retrieval in EDTA buffer (pH 8.0) using a microwave oven. After natural cooling and PBS washes, the sections were blocked with bovine serum albumin (BSA). Following blocking with BSA, the SP1 antibody (21962-1-AP, 1:200, Proteintech) was diluted in PBS, and 50 μL of the monoclonal antibody was added to each section. The sections were incubated overnight at 4 °C. Next, the sections were incubated for 1 h with a CoraLite® 594-conjugated goat anti-rabbit IgG secondary antibody. Finally, DAPI staining was performed, and each section was covered with an appropriate amount of antifade reagent. After sealing, the sections were observed under a fluorescence microscope. Phalloidin staining was performed to visualize F-actin microfilaments for both qualitative and quantitative assessment. Fluorescence intensity of F-actin was measured using ImageJ. For each section, three to five randomly selected, non-overlapping HPFs were analyzed, and the mean fluorescence intensity across these fields was calculated to represent the value for each animal.

Western blot (WB)

Total protein was isolated from cultured cells and subcutaneous tumor tissues using RIPA buffer supplemented with protease inhibitors. Protein samples were separated by SDS–PAGE and then transferred onto PVDF membranes. After blocking, the membranes were incubated sequentially with the primary antibody against SP1 (Cat. No. 21962-1-AP, 1:1000, Proteintech, Wuhan, China) and an HRP-conjugated secondary antibody (Cat. No. AS014, Abclonal, Wuhan, China). Signal detection was performed using an enhanced chemiluminescence system, and band intensities were quantified with Image Lab software (Bio-Rad, Hercules, CA, USA).

Determination of lung hydroxyproline level

At the end of the modeling period, mice were sacrificed and their lungs were excised. The middle and lower lobes of the right lung were collected, and the collagen content of the left lung was determined by measuring hydroxyproline levels. Quantification was performed using a commercial Hydroxyproline Assay Kit (Cat. No. A030-2, Nanjing Jiancheng Bioengineering Institute, Nanjing, China) in accordance with the manufacturer's instructions.

Quantitative real-time PCR

TRIzol reagent (Takara, Japan) was used to extract RNA from cells or lung tissues. RNA purity and concentration were measured using a NanoDrop spectrophotometer (Thermo Fisher Scientific, USA). mRNA expression was quantified by real-time PCR (Prism 7500, ABI, USA) with a commercial RNA reverse transcription kit and real-time PCR kit (Takara). The primer sequences utilized were as follows: Ym1: 5'-CAAAGAACAGTAGATCCTG GCAA-3' (forward), and 5'-ATACCGTGTCCAGACCT TGGT-3' (reverse); α-Sma: 5'-GTCCCAGACATCAGG GAGTAA-3' (forward), and 5'-TCGGATACTTCAGCG TCAGGA-3' (reverse); Ccl2: 5'-ATTCTGTGACCATCC CCTCAT-3' (forward), and 5'-TGTATGTGCCTCTGAA

CCCAC-3' (reverse); Ccl7: 5'-GCTGCTTTCAGCATCC AAGTG-3' (forward), and 5'-CCAGGGACACCGACTA CTG-3' (reverse); Inos: 5'-GAGACAGGGAAGTCTGA AGCAC-3' (forward), and 5'-CAGCAGTGTTGCTCCT CTTC-3' (reverse); Fizz1: 5'-AAGCCTACACTGTGTT TCCTTTT-3' (forward), and 5'-GCTTCCTTGATCCTT TGATCCAC-3' (reverse); Il6: 5'-TACCACTTCACAAGT CGGAGGC-3' (forward), and 5'-CTGCAAGTGCATCA TCGTTGTT-3' (reverse); Cd68: 5'-TGTCTGATCTTGC TAGGACCG-3' (forward), and 5'-GAGAGTAACGGCC TTTTTGTGA-3' (reverse); Cd80: 5'-CTCAAGTTTCCA TGTCCAAGGC-3' (forward), and 5'-GAGGAGAGTTG TAACGGCAAGG-3' (reverse); and Col1a1: 5'-GCTCCT CTTAGGGGCCACT-3' (forward), and 5'-CCACGTCT CACCATTGGGG-3' (reverse). Custom-designed primers were developed and synthesized by Sangon Biotech (Shanghai, China). Data were analyzed using the $2^{-\Delta\Delta Ct}$ method, with β-actin as the internal control.

Statistical analysis and data visualization

Statistical analysis and data visualization were performed using R software (version 4.0.4) and Perl software (version 5.28.1.0). The R packages used for data analysis and visualization included ggplot2, limma, and edgeR. All other statistical analyses were performed using Prism 8.0 software (GraphPad). For the first animal experiment comparing two groups, differences were analysed using Student's t tests. For the second animal experiment involving multiple groups, one-way analysis of variance (ANOVA) was conducted followed by Tukey's multiple comparisons test as the post hoc analysis. Differences were considered statistically significant when $p < 0.05$.

Results

IH exacerbates lung remodelling in mice

We exposed C57BL/6J mice to either IH or normoxia for 6 weeks to investigate the effects of IH on lung tissue. After the exposure period, lung tissues were collected for histopathological staining and analysis. Compared with control mice, those exposed to IH exhibited significant increases in pulmonary inflammation, mucus staining, and collagen deposition (Fig. 1A-D). Phalloidin staining revealed enhanced cytoskeletal organization and increased stress fiber formation, which may reflect actin remodeling associated with both structural cells and infiltrating inflammatory cells in the lungs of IH-exposed mice (Fig. 1A, E). Additionally, histochemical staining revealed increased expression of Cd11b, Mpo, and Cd68 in the lungs of IH-exposed mice, indicating that IH exposure promoted infiltration of immune cells. The upregulation of Cd31 expression in lung tissue further confirmed that IH exposure stimulated remodeling of pulmonary blood vessels (Fig. 1F-G). In summary, IH exposure induced pronounced inflammatory infiltration and structural alterations, contributing to extensive pulmonary tissue and vascular remodeling in mice.

Construction of a single-cell transcriptome map of IH-exposed mouse lungs

Next, we retrieved scRNA-seq data from the GEO database, including lung tissue samples from both IH model mice ($n = 3$) and healthy control mice ($n = 3$), to gain a comprehensive understanding of the cellular landscape in the lung tissue of IH model mice (Supplementary Table 1). After rigorous quality control and filtering, a total of 48,272 cells were retained from the scRNA-seq data for downstream analysis (Supplementary Fig. 1 and Supplementary Table 1). In the scRNA-seq dataset, the median number of unique molecular identifiers (UMIs) per cell was 1978, and the median number of genes detected per cell was 996. After PCA-mediated reduction of these high-quality data, the first 15 PCs were included in the follow-up analysis (Supplementary Fig. 1). We applied the Harmony algorithm to each dataset again to minimize batch effects between different scRNA-seq datasets. Subsequently, we adopted a clustering method based on t-SNE to initially identify 12 clusters according to typical markers of different cell types. These cell types include type 1 alveolar epithelial cells (AT1), type 2 alveolar epithelial cells (AT2), macrophages/monocytes, megakaryocytes, B cells, T cells, fibroblasts, endothelial cells, eosinophils, natural killer (NK) cells, neutrophils, and erythroid cells (Fig. 2A-B, Supplementary Table 2). These cells were present in each sample (Fig. 2E and Supplementary Fig. 1). The specific number of cells identified in each sample is provided in Supplementary Table 2. A total of 195 cells in Clusters 19 and 21 carried markers of two cell types whose expression differed significantly at the same time. We conducted a secondary analysis and divided these 195 cells into three clusters to exclude the possibility of insufficient dimensionality reduction (Fig. 2C). A total of 154 cells in Clusters 0 and 2 expressed endothelial cell and B-cell markers simultaneously. Forty-one cells in Cluster 1 expressed both B-cell and T-cell markers (Fig. 2D-F). We decided not to include these double-positive cells in subsequent analyses to ensure the accuracy and reliability of our results. The calculation of the cell proportion for each cell type indicated significant changes (Fig. 2G). Among all the cells collected, endothelial cells accounted for the largest proportion and exhibited the most obvious increase, and macrophages presented the greatest change among immune cells. Consistent with previous reports, IH exposure increased the number of type 1 alveolar epithelial cells [21]. Notably, IH also promoted the aggregation of fibroblasts in the lung (Fig. 2H) [22, 23].

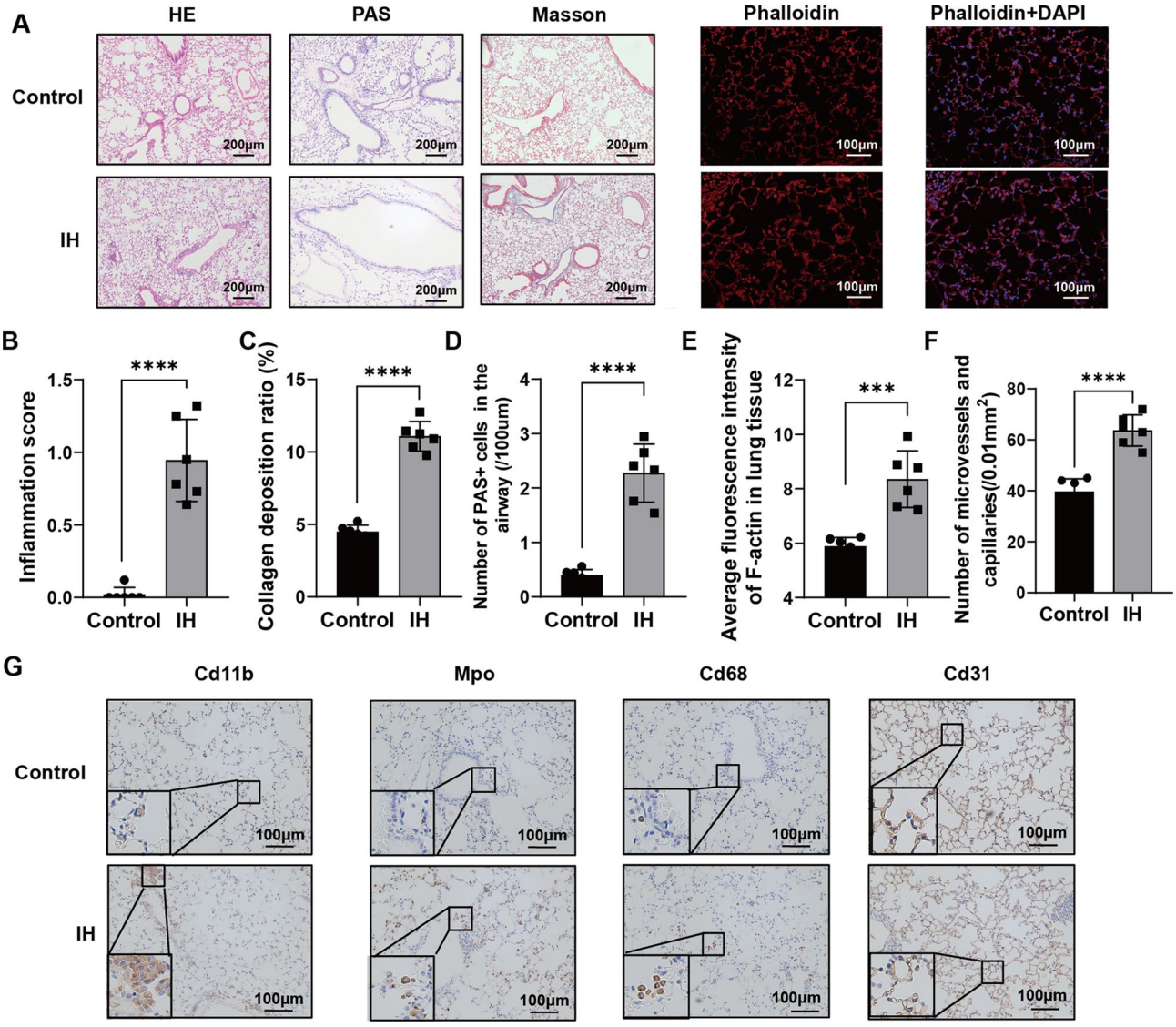

Fig. 1 Pathology of IH-exposed mouse lung tissue ($n = 6$). (**A**) Representative images of H&E and PAS staining, and Masson's trichrome (10× objective) and phalloidin staining (20× objective) in mouse lung tissue. Evaluation of (**B**) the pulmonary airway inflammation score, (**C**) collagen deposition, (**D**) number of PAS^+ cells in the airways, (**E**) remodelling of F-actin in lung tissue in mouse lung tissues.(**F**) Assessment of the level of pulmonary microvascular remodelling. (**G**) Immunohistochemical staining for Cd11b, Mpo, Cd68 and Cd31 in the mouse lungs (20× objective). IH, intermittent hypoxia; PAS, periodic acid–Schiff; Cd11b, cluster of differentiation 11b; MPO, myeloperoxidase; Cd68, cluster of differentiation 68; Cd31, cluster of differentiation 31. The data are presented as the mean ± SD. Statistical significance was assessed using Student's t tests. $^*p < 0.05$, $^{**}p < 0.01$, $^{***}p < 0.001$, $^{****}p < 0.0001$

Characterization of fibroblasts in IH-exposed mouse lungs

Fibroblast heterogeneity was analyzed in scRNA-seq data from six samples (Fig. 3A). Reclustering revealed four fibroblast subtypes (F1-F4) with distinct gene expression profiles (Fig. 3B-C). $Acta2^+$ fibroblasts (F1) expressed high levels of smooth muscle contraction genes such as Actc1 and Myh11 (Fig. 3E), consistent with myoid fibroblasts described previously [24]. GO analysis showed enrichment in actomyosin and muscle system processes for F1 (Fig. 3D). $Tcf21^+$ fibroblasts (F2) highly expressed vascular development genes (Fig. 3E), with GO terms related to blood vessel morphogenesis (Fig. 3D). Dcn^+ fibroblasts (F4) expressed extracellular matrix (ECM) genes (Col1a1, Col3a1) and were enriched in ECM organization pathways (Fig. 3D-E). A proliferative fibroblast cluster (F3) was identified by high ribosomal gene expression and low apoptosis gene expression (Fig. 3E).

Compared to controls, all four fibroblast subtypes expanded after IH exposure, with the most significant increases seen in F1 and F2 cells (Fig. 3F-G). Through transcription factor target analysis, we characterized the predominant regulatory networks in each fibroblast subtype. In F2 and F4 cells, Sp1—a transcription factor involved in transcriptional activation—was predicted to

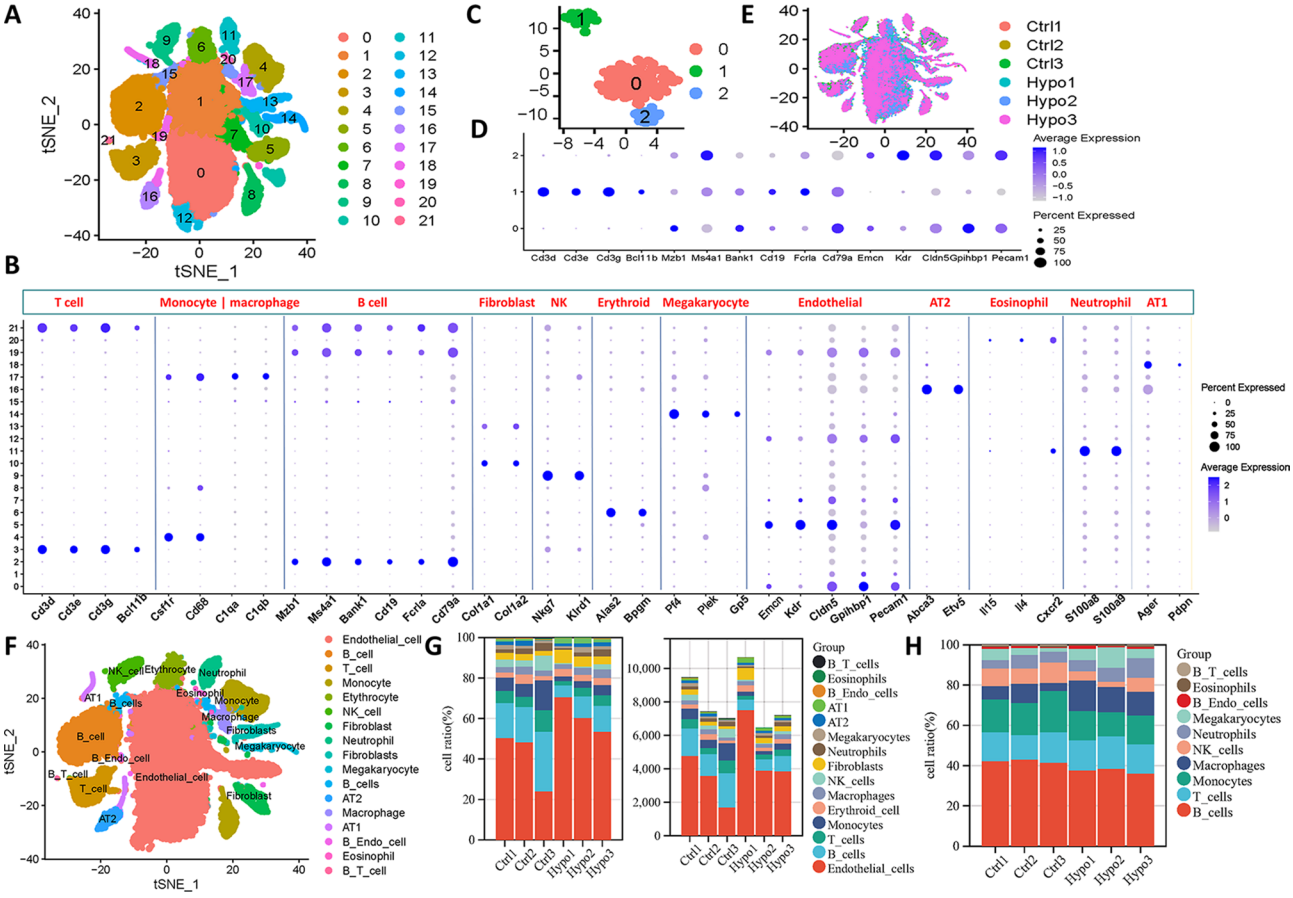

Fig. 2 A single-cell landscape of IH-exposed mouse lungs. (**A**) t-SNE dimensionality reduction analysis of all lung parenchymal cells. (**B**) Bubble maps showing marker genes of different cell clusters. The colour depth of the dots indicates the level of gene expression, and the size of the dots indicates the percentage of cells expressing the corresponding gene. (**C**) Redimensionality reduction and (**D**) cluster marker genes for the 19 and 21 cell clusters. (**E**) Distribution of different cell clusters in different samples. (**F**) Manual annotation of the cell types to which different cell clusters belong. Different colours indicate different cell types. (**G**) Proportions and specific numbers of different types of cells in different samples. (**H**) Proportions of different types of immune cells in different samples. t-SNE, t-distributed stochastic neighbour embedding; AT1, alveolar type 1 cell

regulate numerous target genes. F1 cells were predominantly regulated by serum response factor (Srf), a well-known transcription factor implicated in the contractile phenotype of vascular smooth muscle cells (Fig. 3H) [25]. In F3 cells, Erg was identified as a key regulator, consistent with its known role in fibroblast activation [26]. Gene set scoring revealed F1 fibroblasts had the highest contractility score, F4 fibroblasts the highest ECM score, and F3 the lowest apoptosis score (Fig. 3I). Glycolytic activity scores did not differ significantly among the subtypes. During disease progression, significant proportional changes in fibroblast subtypes were observed. Trajectory analysis showed that F1 and F2 cells were evenly distributed along the developmental timeline, while F4 cells were mainly present during the intermediate stages, and F3 cells were predominantly enriched at the late stages. These trends may explain the greater incidence of hypertension and pulmonary fibrosis in OSAHS patients than in the general population(Fig. 3J-K, Supplementary Fig. 2) [27, 28].

Characterization of monocytes and macrophages in IH-exposed mouse lungs

The t-SNE analysis grouped monocytes and macrophages into 14 clusters based on 2,000 highly variable genes (Fig. 4A, Supplementary Fig. 3). Clusters 0, 5, and 8 were annotated as macrophage subtype 1 (Mϕ1), marked by Wfdc21, Ear1, and Plet1. Clusters 2, 10, 11, and 12 formed monocyte subtype 1 (M1), expressing Treml4 and Cx3cr1, corresponding to nonclassical monocytes. Clusters 3, 4, 6, 7, and 13 were macrophage subtype 2 (Mϕ2), marked by Cd209a, H2-Dmb1, Klrd1, and Ccnd1. Clusters 1 and 9 were monocyte subtype 2 (M2), expressing Ly6c2 and Ccr2, corresponding to classical monocytes (Fig. 4B-C).

Compared to controls, the proportion of M1 cells decreased while Mϕ1 cells increased significantly.

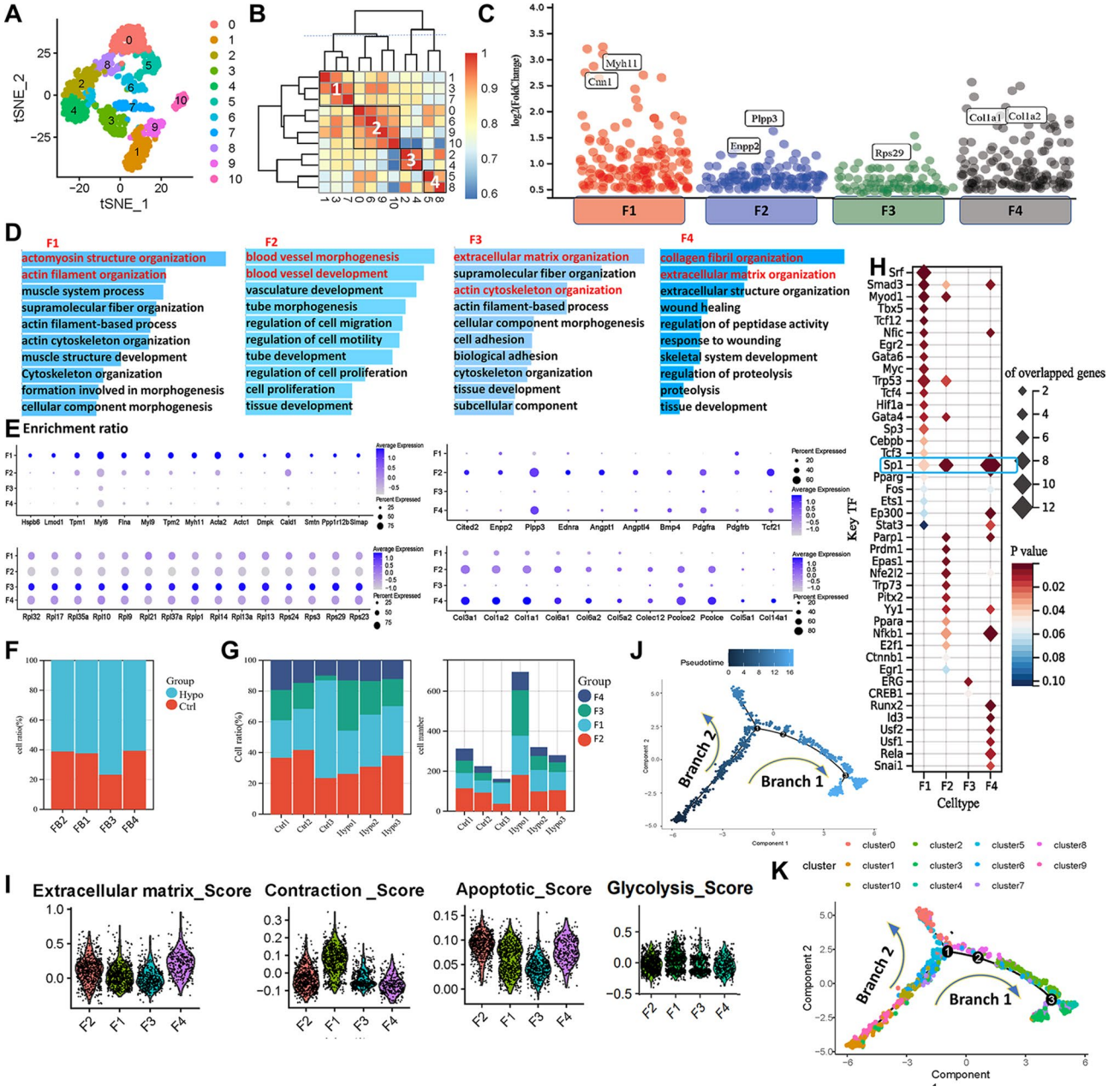

Fig. 3 Characterization of fibroblasts in the lungs of IH-exposed mice. (**A**) Redimensionality analysis of fibroblasts. (**B**) Correlation analysis of different cell clusters. F1 = Cluster 1 + Cluster 3 + Cluster 7, F2 = Cluster 0 + Cluster 6 + Cluster 9 + Cluster 10, F3 = Cluster 2 + Cluster 4, F4 = Cluster 5 + Cluster 8. (**C**) The differential expression analysis indicated the significantly upregulated genes for each fibroblast subtype (adjusted p value < 0.05 & Log FC > 0.5). Cell marker (**E**) and functional enrichment (**D**) analyses of different fibroblast subtypes. The colour depth of the dots indicates the level of gene expression, and the size of the dots indicates the percentage of cells expressing the corresponding gene. (**F**) Proportions of different fibroblast subtypes in different experimental groups. (**G**) Proportions and specific numbers of different types of cells in different samples. (**H**)Bubble map showing the number of predicted transcription factors regulating signature target genes in fibroblast subtypes. (**I**) Violin plot of characteristic scores among different fibroblast subtypes. Pseudotime distribution (**J**) and analysis of the differentiation trajectory (**K**) of different fibroblast clusters. t-SNE, t-distributed stochastic neighbour embedding; F1, myoid fibroblasts; F2, vascular fibroblasts; F3, persistent fibroblasts; F4, matrix fibroblasts

Pseudotime analysis indicated that monocytes progressed from M1 to M2, then to Mϕ2 and ultimately Mϕ1, supporting enhanced monocyte-to-macrophage transition in the lungs under IH exposure (Fig. 4F, Supplementary Fig. 4). Functional scoring revealed that Mϕ1 exhibited the highest fatty acid oxidation and lowest inflammation levels among the four subtypes, while M2 showed the strongest chemotaxis, likely due to recruitment by inflammatory signals. Both macrophage subtypes had lower glycolysis levels than monocytes, and

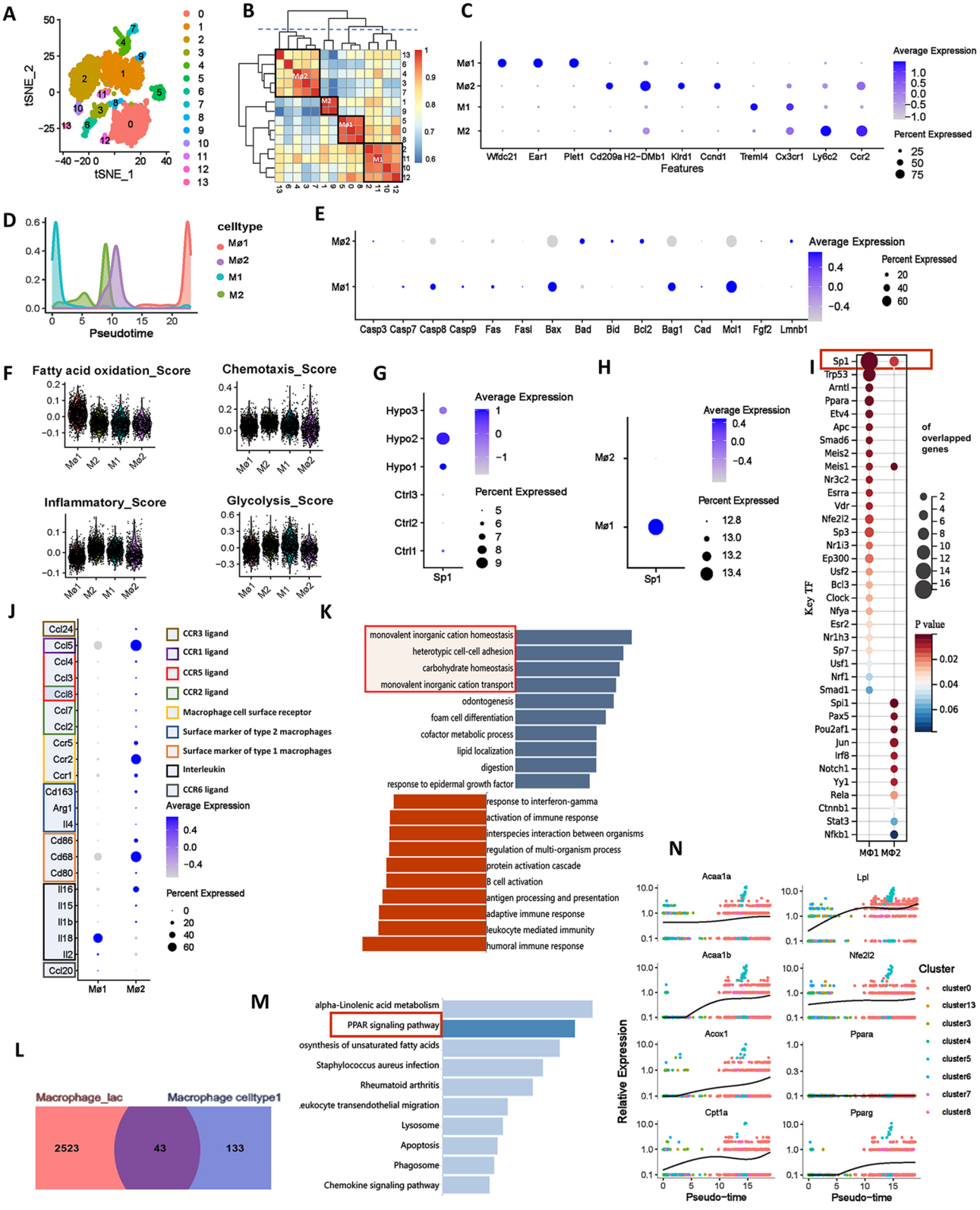

Fig. 4 (See legend on next page.)

(See figure on previous page.)

Fig. 4 Characterization of different subtypes of monocytes and macrophages in IH-exposed mouse lungs. (**A**) t-SNE diagram of monocyte and macrophage redimensionality reduction. (**B**) Correlation analysis of different cell clusters. (**C**) Bubble map showing the marker genes of different cell subtypes. The colour depth of the dots indicates the level of gene expression, and the size of the dots indicates the percentage of cells expressing the corresponding gene. (**D**) Curves showing changes in the distributions of different subtypes of monocytes and macrophages over time. (**E**) Bubble maps of the expression levels of apoptosis-related genes in different subtypes of monocytes and macrophages. (**F**) Violin plot of characteristic scores among different monocyte and macrophage subtypes. (**G**) Bubble map of the amount of Sp1 expressed in different samples. (**H**) Bubble map of Sp1 expression in monocytes and macrophages. The colour depth of the dots indicates the level of gene expression, and the size of the dots indicates the percentage of cells expressing the corresponding gene. (**I**) Bubble map showing the number of predicted transcription factors regulating signature target genes of monocytes and macrophages. (**J**) Cytokine expression levels in different subtypes of macrophages. GSEA (**K**) of Mφ1 characteristic genes. Dark blue represents an FDR < 0.05, and light blue represents an FDR > 0.05 but $p < 0.05$. Venn diagram (**L**) and KEGG enrichment analysis (**M**) of the intersections between Mφ1 signature genes and significantly upregulated genes in lactate-stimulated macrophages. (**N**) Analysis of the developmental trajectory of genes related to the Ppar signalling pathway. t-SNE, t-distributed stochastic neighbour embedding; M1, monocyte subtype 1; Mφ1, macrophage subtype 1; M2, monocyte subtype 2; Mφ2, macrophage subtype 2

Mφ1 displayed disordered apoptosis-related gene expression, suggesting terminal differentiation (Fig. 4E-F). Transcription factor analysis indicated that Sp1 predominantly regulated Mφ1-related genes, with higher expression in the IH group (Fig. 4G-I). GO enrichment showed that M1 was associated with innate immune responses, M2 with immune regulation, Mφ2 with lymphocyte activation, and Mφ1 with lipid metabolism and endocytosis (Supplementary Fig. 4H-K).

Additionally, we analyzed cytokine expression in Mφ1 and Mφ2 from the lungs of IH-exposed mice. The results showed that Mφ1 is characterized by a high expression level of Il18, whereas Mφ2 displayed higher levels of Ccl5, Ccr2, and Cd68, indicative of a classical pro-inflammatory phenotype (Fig. 4J). GSEA of Mφ1 signature genes linked them to processes such as monovalent inorganic cation homeostasis, cell adhesion, and carbohydrate metabolism (Fig. 4K), indicating roles in ion balance and metabolic regulation. KEGG analysis showed significant enrichment of PPAR-related pathways in Mφ1 (Supplementary Fig. 4L), highlighting PPAR's role in metabolism and immune function. Using lactate-treated macrophage data (GSE115354), we found 43 overlapping upregulated genes enriched in PPAR pathways (Fig. 4L-M), confirming PPAR's involvement in IH-induced Mφ1 changes. Expression of key PPAR pathway genes (Acaa1a, Acaa1b, Acox1, Cpt1a, Lpl, Nfe2l2, Pparg) increased over pseudotime (Fig. 4N), indicating enhanced fatty acid oxidation and lipid metabolism in macrophages after IH exposure.

Characterization of T cells in IH-exposed mouse lungs

The t-SNE analysis of scRNA-seq data from six samples revealed the heterogeneity of T cells and identified nine distinct subtypes through clustering (Fig. 5A and B). By calculating the similarity between cell clusters (Fig. 5C), we further classified these clusters into five major subtypes (Fig. 5D). Subtype T1 (Cluster 6) corresponds to exhausted $CD8^+$ T cells, characterized by markers of chronic antigen stimulation and functional exhaustion. Subtype T2 (Clusters 0, 1, 2, 3) represents memory $CD8^+$ T cells with high Cd8a and Ccr7 expression, involved in antigen recognition and immune surveillance. Subtype T3 (Clusters 7, 8) is marked by elevated Gata3, Ccr2, and Cxcr6, consistent with $CD4^+$ Th2 cells that regulate allergic inflammation. Subtype T4 (Cluster 4) shows effector memory features, with Ccl5, Cd8a, and Cxcr3 expression indicating strong migratory and antiviral capacity. Subtype T5 (Clusters 5, 9) comprises regulatory T cells (Tregs), characterized by Foxp3, Ctla4, and Lcos expression, crucial for immune tolerance and suppressing excessive immune responses.

After IH exposure, the proportion of memory T cells (T2) decreased significantly, while $CD4^+$ Th2 cells (T3) increased (Fig. 5F-G). Notably, SP1, a transcriptional regulator linked to T3 signature genes, was significantly upregulated in the IH group, suggesting its role in T3 cell regulation (Fig. 5H). KEGG and GO analyses of T3 highly expressed genes showed enrichment in pathways related to CD4-positive, alpha-beta T-cell differentiation and activation, including Th17 and Th1/Th2 differentiation (Fig. 5I-J). Trajectory analysis showed that T1 and T2 cells were evenly distributed along the developmental timeline, while T4 cells were mainly enriched during the intermediate-to-late stages, and T3 cells were predominantly present at the late stage (Fig. 5L). T3 cells exhibited the highest inflammation score, indicating that their activation and cytokine secretion may exacerbate pulmonary inflammation in late-stage IH (Fig. 5K). Fatty acid oxidation was similar across subtypes, while T1 cells displayed markedly lower glycolysis, consistent with an exhausted phenotype. These findings demonstrate that IH reshapes T-cell composition and function, promoting Th2-skewed inflammation and T-cell exhaustion.

Characterization of endothelial cells in IH-exposed mouse lungs

We analyzed endothelial cells from six samples using scRNA-seq data. t-SNE analysis identified nine clusters (Fig. 6A), which were grouped into five subtypes based on cluster similarity (Fig. 6B): endo1 (Clusters 1 and 5), endo2 (Clusters 1, 3, and 4), endo3 (Clusters 6, 7, and 9), endo4 (Cluster 0), and endo5 (Cluster 8). The distribution of these subtypes across samples is shown in Fig. 6C and D. Marker gene analysis revealed distinct

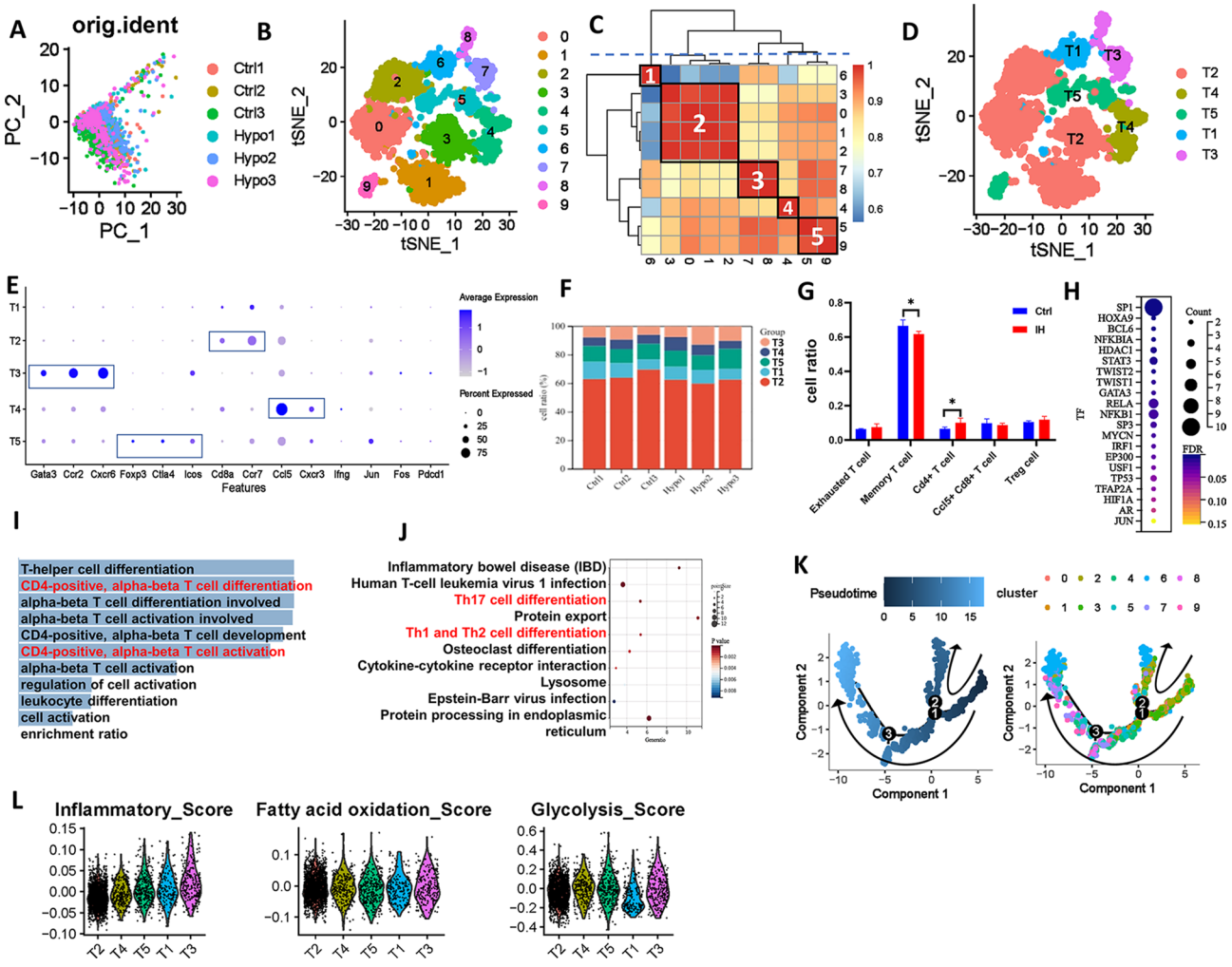

Fig. 5 Characterization of different subtypes of T cells in IH-exposed mouse lungs. (**A**) PCA diagram of T-cell redimensionality reduction. (**B**) t-SNE diagram of T-cell redimensionality reduction. (**C**) Correlation analysis of different cell clusters. (**D**) t-SNE distribution of different subtypes of T cells. (**E**) Bubble map showing the marker genes of different T-cell subtypes. (**F**) and (**G**) Distribution of different T-cell subtypes in different samples. (**H**) Bubble map showing the number of predicted transcription factors regulating signature target genes of T3 cell. KEGG (**I**) and GO enrichment analyses (**J**) of highly expressed genes in T3 cells. (**K**) Analyses of the differentiation trajectory and pseudotime distribution of different clusters of T cells. (**L**) Violin plot of the characteristic scores among different T-cell subtypes. PCA, principal component analysis; t-SNE, t-distributed stochastic neighbour embedding

profiles: Cyb5r3 and Rps29 for endo1; Cldn5 and Foxf1 for endo2; Emp2 and Cdh5 for endo3; Vwf and Cytl1 for endo4, consistent with venous endothelial cells [29]; and Ccl21a and Mmrn1 for endo5, matching lymphatic endothelial cell signatures (Fig. 6E) [29]. Among these, endo2 was the most abundant, while endo5 was the least prevalent. Notably, IH exposure increased the proportions of endo1 to endo3 cells (Fig. 6F). Pseudotime trajectory analysis revealed a dynamic transition of endothelial subtypes over time: endo2 and endo5 predominated in the early stages, endo3 was evenly distributed throughout the trajectory, and endo1 and endo4 became dominant at the terminal stage (Fig. 6G, Supplementary Fig. 5). KEGG enrichment analysis demonstrated subtype-specific functional programs: endo1 was enriched in "ribosome" and "oxidative phosphorylation"; endo2 in "antigen processing and presentation" and "fluid shear stress and atherosclerosis"; endo3 in "IL-4/IL-13 signaling" and "apoptosis"; endo4 in "TGF-beta signaling" and "stem cell pluripotency"; and endo5 in "ferroptosis" and "autophagy" (Fig. 6H). These findings suggest that during IH exposure, endothelial cells undergo functional reprogramming from immune and stress responses toward a more reparative and metabolically active phenotype.

Analysis of interactions between monocytes/macrophages and other altered cell types

We analyzed receptor–ligand interactions between monocytes/macrophages and other altered cell types to further elucidate the cellular interactions within lung tissue exposed to IH. The results revealed that the interactions between the endo2 and other cell

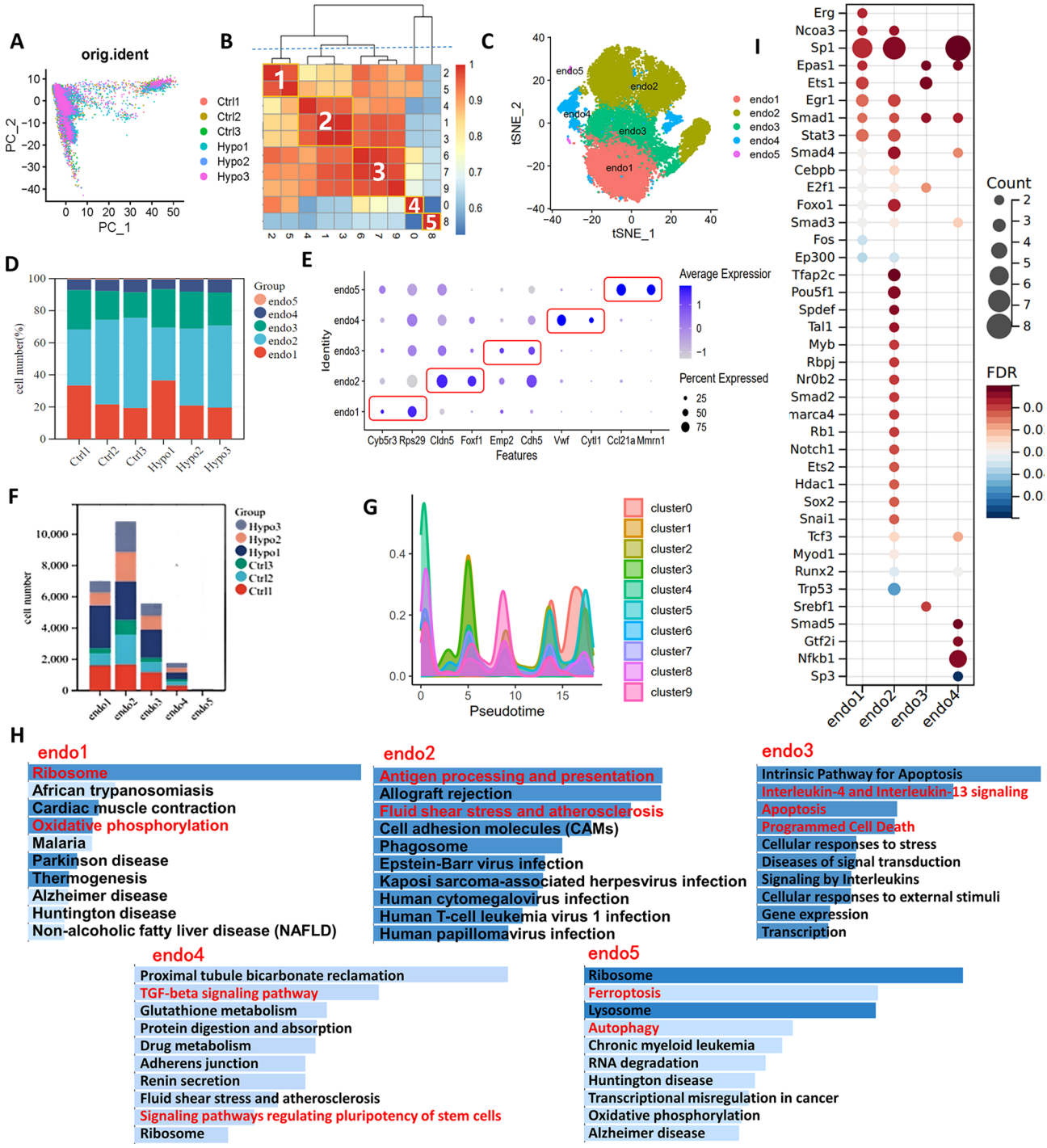

Fig. 6 Characterization of different subtypes of endothelial cells in IH-exposed mouse lungs. (**A**) t-SNE diagram of endothelial cell redimensionality reduction. (**B**) Correlation analysis of different endothelial cell clusters. Endo1 = Cluster 2 + Cluster 5, endo2 = Cluster 1 + Cluster 3 + Cluster 4, endo3 = Cluster 6 + Cluster 7 + Cluster 9, endo4 = Cluster 0, endo5 = Cluster 8. (**C**) t-SNE distribution of different subtypes of endothelial cells. (**D**) The distribution of different endothelial cell subtypes in different samples. (**E**) Bubble map showing the marker genes of different endothelial cell subtypes. (**F**) The specific numbers of different endothelial cell subtypes in different samples. (**G**) Curves showing the distributions of different subtypes of endothelial cells over time. (**H**) KEGG enrichment analysis of characteristic genes of different endothelial cell subtypes. (**I**) Bubble map showing the number of predicted transcription factors regulating signature target genes of different endothelial cell subtypes. PCA, principal component analysis

subtypes were particularly strong. Among these interactions, endo2 cells exhibited similarly strong interactions with both Mϕ1 and M2 , and these interactions were markedly stronger than those observed with other cell types (Fig. 7A and B). Additionally, interactions between Tgfb1–(Tgfbr1 + Tgfbr2), Ccl6–Ccr2, Sema3a–(Nrp1 + Plxna2), and Sema3c–(Nrp1 + Plxna2) are highly probable within the network of monocytes/macrophages and other altered cell types, with Ccl6–Ccr2 showing the strongest potential for interaction. Notably, the receptor for Ccl6, Ccr2, was expressed in multiple cell subtypes, with prominent expression in endothelial cells and macrophage/monocyte-related subtypes (Fig. 7E). We performed immunohistochemistry to investigate this phenomenon further, and the results confirmed that Ccr2 expression was indeed upregulated in the lung tissue of the IH-exposed group (Fig. 7F), suggesting that Ccr2 may play a significant role in the pathophysiology of IH.

Effect of the SP1 intervention on the lung tissue of IH-Exposed mice

In this study, we first confirmed that SP1 expression was significantly upregulated in the lungs of mice exposed to IH, as evidenced by both immunofluorescence staining and western blot analysis (Fig. 8A-D). Based on this observation, we established an IH mouse model combined with the SP1 inhibitor plicamycin to further investigate its therapeutic potential. Western blot analysis and immunofluorescence analysis (Fig. 8E-F and H-I) showed that plicamycin treatment partially reversed the IH-induced upregulation of SP1 in lung tissue. Similarly, measurement of lung hydroxyproline levels suggested a modest reduction following plicamycin treatment compared with IH alone (Fig. 8G). Subsequently, histopathological evaluation revealed that plicamycin tended to attenuate IH-induced pulmonary inflammation, mucus secretion, and collagen deposition (Fig. 8H and J–L), indicating that SP1 plays a central role in mediating lung injury under IH exposure. Additionally, phalloidin staining revealed increased F-actin remodeling and stress fiber

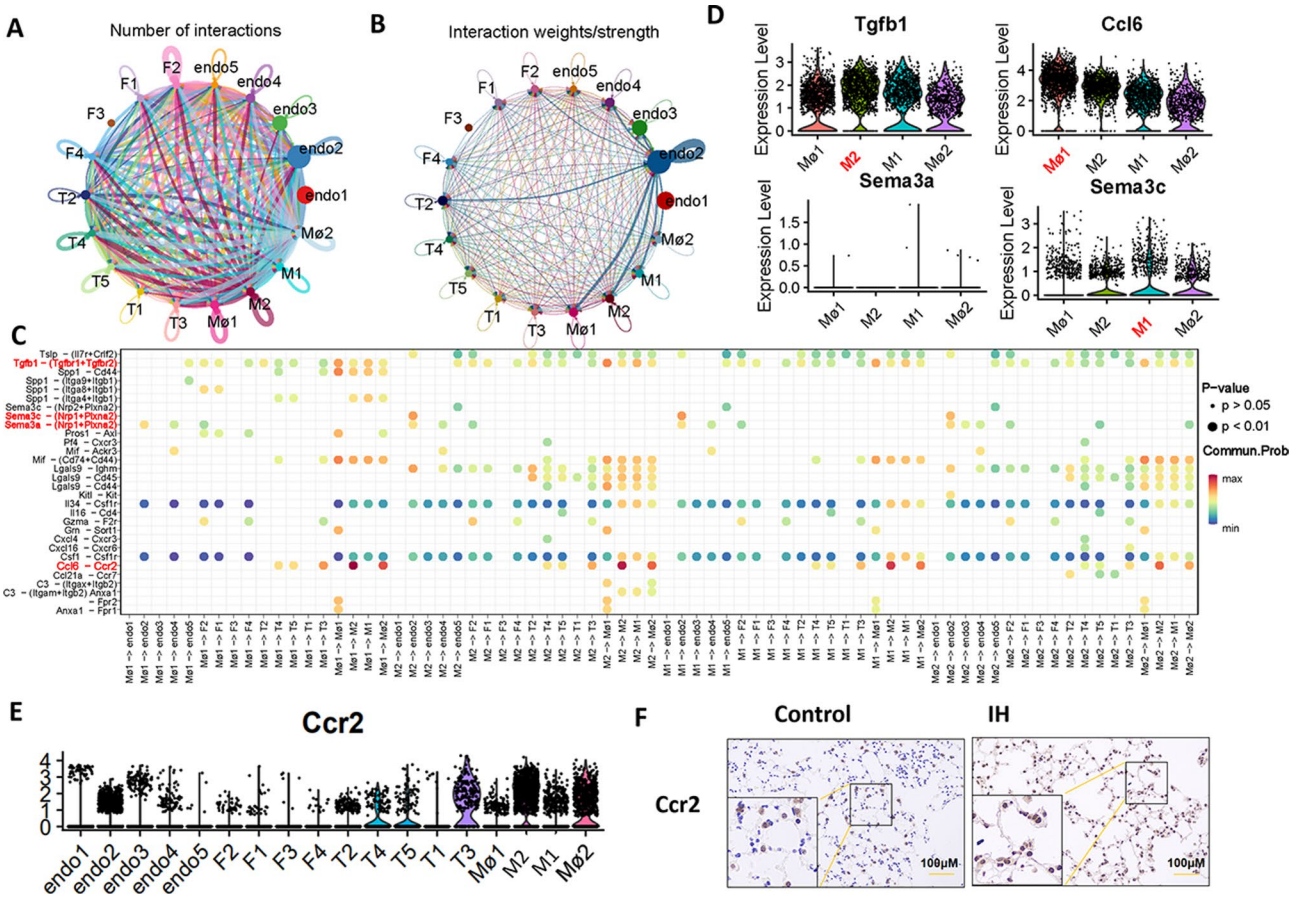

Fig. 7 Analysis of interactions between different cell subtypes. (**A**, **B** and **C**) Receptor–ligand interactions between monocytes, macrophages, endothelial cells, and fibroblast subtypes. (**D**) Violin plot showing the expression levels of Tgfb1, Ccl6, Sema3a and Sema3c in different monocyte/macrophage subtypes. (**E**) Violin plot showing the expression levels of Ccr2 in different cell types. (**F**) Immunohistochemical staining for Ccr2 in the mouse lungs (20× objective). IH, intermittent hypoxia; Ccr2, C-C chemokine receptor type 2

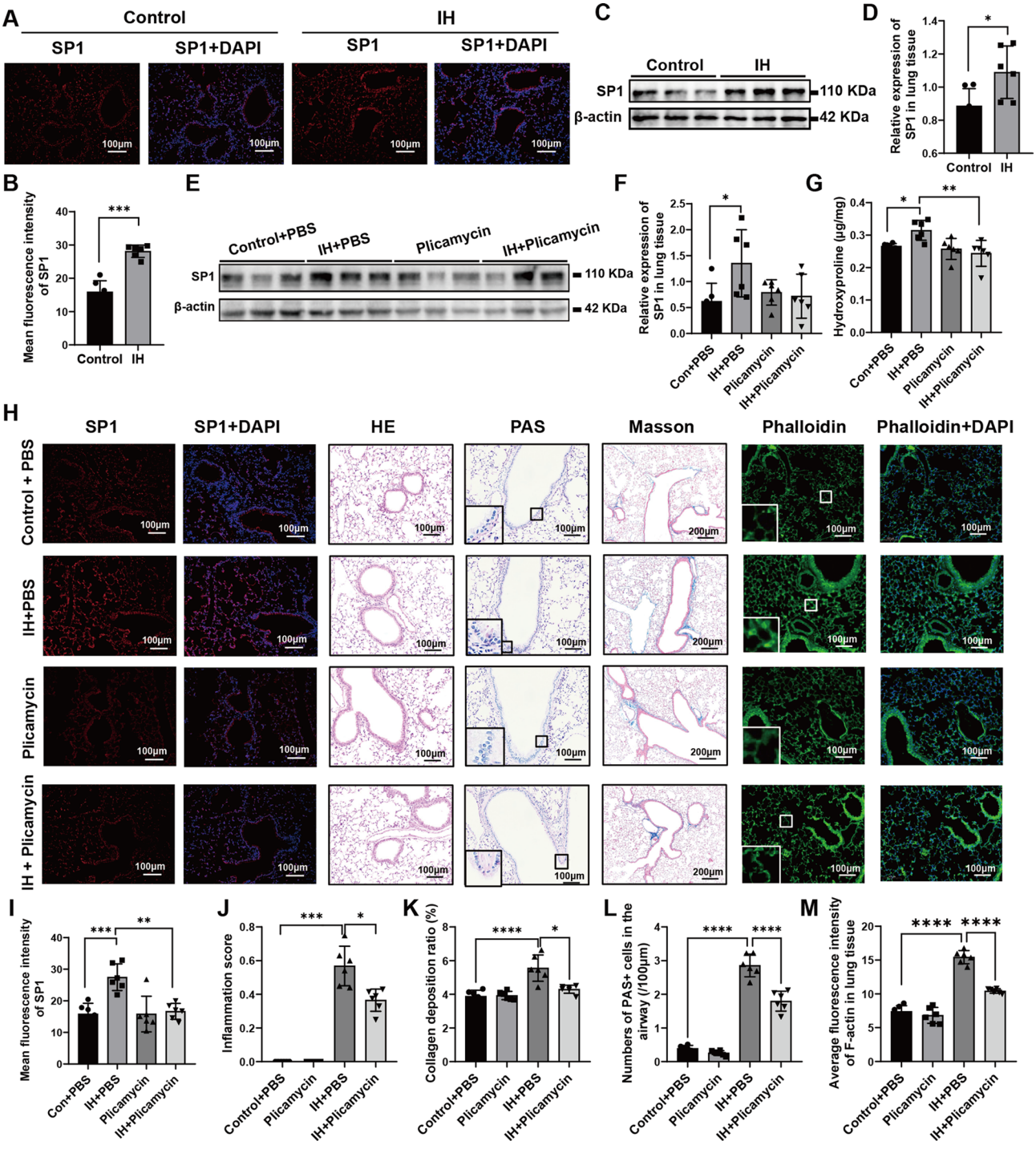

Fig. 8 SP1 expression and the effect of plicamycin on lung tissue in mice exposed to intermittent hypoxia ($n = 6$). (**A**) Immunofluorescence staining of SP1 (red) and nuclei (blue, DAPI) in lung tissues from Control and IH groups. (**B**) Quantification of mean fluorescence intensity of SP1 in (**A**). (**C**) Western blot analysis of SP1 protein expression in lung tissues from Control and IH groups, with β-actin as a loading control. (**D**) Quantitative analysis of relative SP1 protein expression in (**C**). (**E**) Western blot analysis of SP1 protein expression in lung tissues from Control + PBS, IH + PBS, Plicamycin, and IH + Plicamycin groups, with β-actin as a loading control. (**F**) Quantitative analysis of relative SP1 protein expression in (**E**). (**G**) Measurement of hydroxyproline content in lung tissues from different groups. (**H**) Representative images showing SP1 expression (immunofluorescence, SP1 in red, DAPI in blue), HE staining, PAS staining, Masson's trichrome staining (10× objective, others 20× objective), and phalloidin staining (phalloidin in green, DAPI in blue) in lung tissues from four groups (Control + PBS, IH + PBS, Plicamycin, IH + Plicamycin) (objective magnifications: 10× or 20×, as indicated). (**I**) Quantification of mean fluorescence intensity of SP1 in (**H**). (**J**) Airway inflammation score based on HE staining. (**K**) Collagen deposition ratio assessed by Masson's trichrome staining. (**L**) Number of PAS$^+$ cells in the airways. (**M**) Average fluorescence intensity of F-actin (phalloidin staining) in lung tissue. IH, intermittent hypoxia; HE, haematoxylin and eosin; PAS, periodic acid–Schiff; The data are presented as the mean ± SD. Statistical analysis was performed using one-way analysis of variance (ANOVA) followed by Tukey's multiple comparisons test as post hoc analysis. *$p < 0.05$, **$p < 0.01$, ***$p < 0.001$, ****$p < 0.0001$

formation in the lungs of IH-exposed mice, which was partially alleviated by plicamycin treatment (Fig. 8H and M). Furthermore, PCR analysis revealed that plicamycin effectively reduced the expression of genes involved in inflammation and fibrosis, including Fizz1, Ym1, Il6, α-Sma, Cd68, Ccl2, Cd80, Ccl7, Col1a1, and iNOS (Supplementary Fig. 6 A), further suggesting that SP1 plays a key role in pulmonary inflammation and fibrosis induced by IH exposure. In conclusion, the SP1 inhibitor plicamycin significantly suppresses the inflammatory response, cytoskeletal remodeling, and fibrosis in the lung tissue of IH-exposed mice.

Discussion

IH, a hallmark of OSAHS, has profound effects on various pulmonary diseases, particularly in promoting lung tissue remodeling. For example, previous studies have shown that IH can promote airway remodeling in asthma [20]. Additionally, chronic IH has been linked to pulmonary inflammation and small artery remodeling, potentially due to oxidative stress [13]. In this study, we performed a comprehensive single-cell transcriptome analysis of lung tissue from mice exposed to IH, revealing significant changes in key cell types and pathways. In addition, our study confirmed that IH exposure significantly exacerbated lung tissue remodeling, with increased inflammation, mucus production, and collagen deposition.

First, we performed a high-resolution scRNA-seq analysis to better understand the cellular landscape of IH-induced lung remodeling. One interesting finding was that the myoid fibroblast and vascular fibroblast populations, which are involved in vascular and smooth muscle remodeling [24, 30], showed particularly significant expansion in response to IH, suggesting that IH may drive fibroblasts to transition into distinct functional states, contributing to fibrosis and vascular remodeling. Further analysis revealed that the differentiation of these fibroblast subtypes was closely linked to the enrichment of specific transcription factors and transcriptional activators, particularly Sp1 and Srf, in the vascular fibroblast and persistent fibroblast subtypes. Sp1 is a well-studied transcription factor that is known to play crucial roles in cell proliferation, differentiation, and fibrosis [31–33]. Srf is a key regulator of vascular smooth muscle cell (VSMC) contractility and plays an important role in vascular remodeling and fibrosis [25, 34–36]. These findings suggest that IH-induced lung remodeling may be driven by the modulation of fibroblast differentiation and the expression of key genes involved in fibrosis and vascular remodeling.

Moreover, the scRNA-seq analysis revealed that IH exposure accelerated the transition of monocytes and macrophages, resulting in the accumulation of Mϕ1 cells (characterized by high IL-18 expression) in the lung. These findings align with previous studies showing that IH promotes proinflammatory macrophage polarization, leading to chronic inflammatory diseases [37–39]. Additionally, the analysis of regulatory genes identified Sp1 as a key transcription factor enriched in Mϕ1 cells, and we observed significant activation of the PPAR signaling pathway upon IH exposure. These results further highlight the central role of Sp1 in IH-induced pathological processes, and the PPAR pathway may serve as a potential therapeutic target for IH-induced pulmonary diseases.

We also analyzed the T-cell populations in IH-exposed mouse lungs. We found that IH exposure decreased the proportion of memory T cells (T2) and increased the proportion of $CD4^+$ T cells (T3), which shifted towards a more proinflammatory phenotype. The increase in the number of $CD4^+$ T cells is consistent with several studies showing IH-induced alterations in T-cell populations [40, 41]. Interestingly, the analysis of apoptosis-related genes revealed that T3 cells exhibited lower apoptotic activity than T1 cells, which exhibited increased apoptosis in the later stages of IH exposure. These findings suggest that T3 cells play a role in immune regulation and tolerance, whereas T1 cells are more involved in aggressive cytotoxic immune responses, possibly due to increased turnover and apoptosis. Some studies have suggested that IH exposure suppresses the cytotoxic activity of $CD8^+$ T cells [42], and in tumor environments, IH exposure can lead to a reduction in the number of $CD8^+$ T cells that release cytolytic enzymes (e.g., granzyme B)[43]. These findings reflect the functional changes in T cells induced by IH. However, further analysis of $CD8^+$ T-cell function and the underlying mechanisms is needed in the future.

We also analyzed the endothelial cell response to IH exposure, identifying five distinct subtypes (endo1, endo2, endo3, endo4, and endo5) with dynamic changes upon IH exposure, with endo2 being the most abundant. Additionally, analysis of receptor–ligand interactions in IH-exposed lung tissue revealed significant interactions, particularly between the endo2 endothelial cell subtype and monocytes/macrophages. These findings suggest that endothelial cells and monocytes/macrophages play key roles in the inflammatory response to IH, contributing to tissue remodeling and fibrosis. We also identified that Tgfb1–(Tgfbr1 + Tgfbr2), Ccl6–Ccr2, Sema3a–(Nrp1 + Plxna2), and Sema3c–(Nrp1 + Plxna2) interactions are central to the interaction network between various cell subtypes, with Ccl6–Ccr2 exerting the most significant influence. Ccr2, the receptor for Ccl6, is expressed in nearly all circulating monocytes and plays a crucial role in their chemotaxis to inflamed sites, and Ccr2 expression is upregulated after IH exposure [44, 45]. Our results also showed that Ccr2 was upregulated in all cell subsets in IH-exposed lung tissue, further suggesting that Ccr2

signaling may play a key role in the pathophysiology of IH.

Finally, we investigated the role of SP1 in IH-induced lung injury in mice. SP1 expression was significantly upregulated in the lungs of IH-exposed mice, as shown by immunofluorescence and Western blot analyses. Treatment with the SP1 inhibitor plicamycin reduced SP1 expression and attenuated IH-induced lung inflammation, mucus secretion, and collagen deposition, as indicated by hydroxyproline measurements. Plicamycin also alleviated cytoskeletal remodeling and decreased the expression of inflammation- and fibrosis-related genes, including Il6 and Col1a1. These results indicate that SP1 is a key mediator of IH-induced lung injury and that its inhibition may represent a potential therapeutic strategy for IH-related pulmonary diseases.

Despite the valuable insights gained from this study, several limitations should be considered. First, while we used a mouse model to study the effects of IH exposure on lung tissue, species differences may limit the direct translation of these findings to human diseases. Second, although single-cell RNA sequencing captures transcriptional changes, it cannot fully reflect post-transcriptional or protein-level modifications. Future studies should incorporate proteomics and in vivo validation to confirm whether these transcriptional changes correspond to biological functions or pathological alterations. Third, while our study identified SP1-related transcriptional alterations in multiple cell types, functional validation was only performed at the whole-lung level using pharmacological intervention. Further lineage-specific functional studies (e.g., fibroblasts, macrophages, endothelial cells) are needed to dissect the precise cellular mechanisms by which SP1 contributes to IH-induced remodeling. Finally, although plicamycin was used as a pharmacological inhibitor of SP1 and has been reported to block SP1 binding to GC-rich promoter regions, it may also exert off-target effects on other GC-binding transcription factors. As such, future studies employing SP1-targeted genetic approaches are warranted to confirm its mechanistic role in IH-induced pulmonary remodeling and to better evaluate its therapeutic potential.

Conclusions

This study utilized single-cell RNA sequencing to analyze lung tissue from mice exposed to IH, revealing significant changes in key cell types and pathways. IH exposure led to fibroblast differentiation linked to fibrosis and vascular remodeling, monocyte/macrophage polarization to a proinflammatory phenotype, and T-cell alterations, particularly involving the SP1 transcription factor. These findings improve our understanding of the mechanisms underlying OSAHS and other IH-related pulmonary diseases. This study also identified potential therapeutic targets, such as the SP1 and PPAR pathways, to address IH-induced lung injury. Despite certain limitations, this research provides valuable insights into the cellular and molecular effects of IH exposure, laying the groundwork for future therapeutic interventions.

Abbreviations

Acta2	Smooth muscle actin
Actc1	actin alpha cardiac muscle 1
Angpt1	Angiopoietin 1
Angptl4	Angiopoietin-like 4
ANOVA	One-way analysis of variance
BSA	Bovine serum albumin
BMP4	Bone morphogenetic protein 4
Cald1	Calmodulin 1
Ccr2	C-C chemokine receptor type 2
Cd68	Cluster of differentiation 68
Cd31	Cluster of differentiation 31
Cd11b	Cluster of differentiation 11b
Colec12	C1q domain containing 12
Col1a1	Collagen type I alpha 1 chain
Col1a2	Collagen type I alpha 2 chain
Col3a1	Collagen type III alpha 1 chain
Col6a1	Collagen type VI alpha 1 chain
Col6a2	Collagen type VI alpha 2 chain
Dcn	Collagen-forming gene
Enos	Endothelial nitric oxide synthase
Erg	Ets related gene
F-actin	Filamentous actin
Flna	Filamin A
GEO	Gene expression omnibus
GO	Gene ontology
GSEA	Gene set enrichment analysis
HE	Hematoxylin and eosin
IH	Intermittent hypoxia
M1	Monocyte subtype 1
Mφ1	Macrophage subtype 1
Masson	Masson's Trichrome Staining
Mpo	Myeloperoxidase
Myh11	Myosin heavy chain 11
Myl6	Myosin light chain 6
OSAHS	Obstructive sleep apnea-hypopnea syndrome
PAS	Periodic acid-schiff
PCA	Principal component analysis
Pdgfrb	Platelet-derived growth factor receptor betaβ
Pcolec2	Procollagen type I c-terminal propeptide
Rpl10-ps3	Ribosomal protein L10-PS3
Rpl11	Ribosomal protein L11
Rpl13a	Ribosomal protein L13a
Rpl14	Ribosomal protein L14
Rpl35a	Ribosomal protein L35a
Rpl9	Ribosomal protein L9
Rplp1	Ribosomal protein L1
Srf	Smooth muscle regulating factor
SP1	Specificity protein 1
t-SNE	t-distributed stochastic neighbor embedding

Supplementary Information

The online version contains supplementary material available at https://doi.org/10.1186/s12931-025-03370-y.

Supplementary Material. The quality control of single-cell sequencing data, pseudo-temporal analysis of fibroblast, monocyte, macrophage, and endothelial clusters, and the landscape of monocytes and macrophages in IH-exposed mouse lungs, also includes Supplementary Tables 1–2, which provide dataset metadata (GSE145435) and cell counts per sample (docx).

Authors' contributions
P.Z. and L.W. designed the study, developed the experimental protocols, conducted key experiments, collected data, and drafted the initial manuscript. X.Z. developed and implemented the data analysis software, performed statistical analyses, and generated the visualizations for figures. Z.M. and F.Z. were responsible for data management, performed detailed data curation, and conducted independent formal analysis to validate the results. G.Z. and L.C. provided essential laboratory resources, contributed to sample preparation, and participated in experimental investigations. H.L., L.Z., and W.L. supervised the overall project, provided critical revisions to the manuscript, and ensured the integrity of the research process through project administration. All authors critically reviewed, commented on, and approved the final version of the manuscript. P.Z. and L.W. contributed equally to this work.

Funding
This work was supported by the Noncommunicable Chronic Diseases–National Science and Technology Major Project (2024ZD0541700, 2023ZD0506700); the National Natural Science Foundation of China (82270104); the Health Commission of Hubei Province Scientific Research Project (WJ2023Z010, WJ2025M015); the Hubei Provincial Natural Science Foundation (2024AFB050, 2025AFB057); the Postdoctor Project of Hubei Province under Grant Number (2024HBBHCXB025); the Natural Science Foundation of Wuhan (2024040801020345); and the Tongji Hospital Fund Cultivation Project (2024B10, 2024B26).

Data availability
The dataset analyzed in this study was obtained from the publicly available GEO repository under accession number [GSE145435], accessible at https://www.ncbi.nlm.nih.gov/geo/query/acc.cgi? acc=GSE145435. Other data supporting the findings of this study are available from the corresponding author upon reasonable request.

Declarations

Ethics approval and consent to participate
All animal procedures were approved by the Institutional Animal Care and Use Committee of Tongji Hospital and performed in accordance with the National Guidelines for Animal Welfare (China) and NIH Guide for the Care and Use of Laboratory Animals.

Consent for publication
N/A.

Competing interests
The authors declare no competing interests.

Author details
[1]Department of Respiratory and Critical Care Medicine, Key Laboratory of Respiratory Disease, Tongji Hospital, Tongji Medical College, National Health Commission (NHC), Huazhong University of Science and Technology, Wuhan 430030, China
[2]Hubei Branch of National Clinical Research Center for Infectious Diseases, Wuhan Pulmonary Hospital (Wuhan Tuberculosis Prevention and Control Institute), Wuhan 430030, China
[3]Department of Geriatrics, Key Laboratory of Vascular Aging, Ministry of Education, Tongji Hospital, Tongji Medical College, Huazhong University of Science and Technology, No. 1095 Jiefang Avenue, Wuhan 430030, China

Received: 14 April 2025 / Accepted: 25 September 2025
Published online: 28 October 2025

References

1. Lévy P, Kohler M, McNicholas WT, et al. Obstructive sleep Apnoea syndrome. Nat Rev Dis Primers. 2015;1:15015. https://doi.org/10.1038/nrdp.2015.15.
2. Benjafield AV, Ayas NT, Eastwood PR, et al. Estimation of the global prevalence and burden of obstructive sleep apnoea: a literature-based analysis. Lancet Respir Med. 2019;7:687–98. https://doi.org/10.1016/S2213-2600(19)30198-5.
3. Lv R, Liu X, Zhang Y, et al. Pathophysiological mechanisms and therapeutic approaches in obstructive sleep apnea syndrome. Signal Transduct Target Ther. 2023;8:218. https://doi.org/10.1038/s41392-023-01496-3.
4. Redline S, Azarbarzin A, Peker Y. Obstructive sleep Apnoea heterogeneity and cardiovascular disease. Nat Rev Cardiol. 2023;20:560–73. https://doi.org/10.1038/s41569-023-00846-6.
5. Rodriguez J, Escobar JB, Cheung EC et al. Hypothalamic Oxytocin Neuron Activation Attenuates Intermittent Hypoxia-Induced Hypertension and Cardiac Dysfunction in an Animal Model of Sleep Apnea. *Hypertension (Dallas, Tex.*: 1979) 80, 882–894. https://doi.org/10.1161/hypertensionaha.122.20149 (2023).
6. Mesarwi OA, Loomba R, Malhotra A. Obstructive sleep Apnea, Hypoxia, and nonalcoholic fatty liver disease. Am J Respir Crit Care Med. 2019;199:830–41. https://doi.org/10.1164/rccm.201806-1109TR.
7. Mesarwi OA, Moya EA, Zhen X, et al. Hepatocyte HIF-1 and intermittent hypoxia independently impact liver fibrosis in murine nonalcoholic fatty liver disease. Am J Respir Cell Mol Biol. 2021;65:390–402. https://doi.org/10.1165/rcmb.2020-0492OC.
8. Badran M, Khalyfa A, Ericsson AC, et al. Gut microbiota mediate vascular dysfunction in a murine model of sleep apnoea: effect of probiotics. Eur Respir J. 2023;61. https://doi.org/10.1183/13993003.00002-2022.
9. O'Connor KM, Lucking EF, Bastiaanssen TFS, et al. Prebiotic administration modulates gut microbiota and faecal short-chain fatty acid concentrations but does not prevent chronic intermittent hypoxia-induced Apnoea and hypertension in adult rats. EBioMedicine. 2020;59:102968. https://doi.org/10.1016/j.ebiom.2020.102968.
10. Correia MJ, Pimpão AB, Lopes-Coelho F, et al. Aryl hydrocarbon receptor and cysteine redox dynamics underlie (Mal)adaptive mechanisms to chronic intermittent hypoxia in kidney cortex. Antioxid (Basel Switzerland). 2021;10. https://doi.org/10.3390/antiox10091484.
11. Gong LJ, Wang XY, Gu WY, Wu X. Pinocembrin ameliorates intermittent hypoxia-induced neuroinflammation through BNIP3-dependent mitophagy in a murine model of sleep apnea. J Neuroinflamm. 2020;17. https://doi.org/10.1186/s12974-020-02014-w.
12. Liu W, Pu L, Deng B, et al. Intermittent hypobaric hypoxia causes deleterious effects on the reproductive system in female rats. Biomed pharmacotherapy = Biomedecine Pharmacotherapie. 2020;130:110511. https://doi.org/10.1016/j.biopha.2020.110511.
13. Song JQ, Jiang LY, Fu CP, et al. Heterozygous SOD2 deletion deteriorated chronic intermittent hypoxia-induced lung inflammation and vascular remodeling through mtROS-NLRP3 signaling pathway. Acta Pharmacol Sin. 2020;41:1197–207. https://doi.org/10.1038/s41401-019-0349-y.
14. Wu G, Lee YY, Gulla EM, et al. Short-term exposure to intermittent hypoxia leads to changes in gene expression seen in chronic pulmonary disease. eLife. 2021;10. https://doi.org/10.7554/eLife.63003.
15. Zheng P, Zhang H, Jiang W, et al. Establishment of a prognostic model of lung adenocarcinoma based on tumor heterogeneity. Front Mol Biosci. 2022;9:807497. https://doi.org/10.3389/fmolb.2022.807497.
16. Lall S, Sinha D, Bandyopadhyay S, Sengupta D. Structure-Aware principal component analysis for Single-Cell RNA-seq data. J Comput Biology: J Comput Mol Cell Biology. 2018. https://doi.org/10.1089/cmb.2018.0027.
17. Satija R, Farrell JA, Gennert D, Schier AF, Regev A. Spatial reconstruction of single-cell gene expression data. Nat Biotechnol. 2015;33:495–502. https://doi.org/10.1038/nbt.3192.
18. Qiu X, Hill A, Packer J, et al. Single-cell mRNA quantification and differential analysis with census. Nat Methods. 2017;14:309–15. https://doi.org/10.1038/nmeth.4150.
19. Zhang H, Zhou L, Zhou Y, et al. Intermittent hypoxia aggravates non-alcoholic fatty liver disease via RIPK3-dependent necroptosis-modulated Nrf2/NFκB signaling pathway. Life Sci. 2021;285:119963. https://doi.org/10.1016/j.lfs.2021.119963.
20. Zhou JP, Wang Y, Li SQ, et al. Exogenous Ang-(1–7) inhibits autophagy via HIF-1α/THBS1/BECN1 axis to alleviate chronic intermittent hypoxia-enhanced airway remodelling of asthma. Cell Death Discovery. 2023;9:366. https://doi.org/10.1038/s41420-023-01662-0.
21. Reinke C, Bevans-Fonti S, Grigoryev DN, et al. Chronic intermittent hypoxia induces lung growth in adult mice. Am J Physiol Lung Cell Mol Physiol. 2011;300:L266–273. https://doi.org/10.1152/ajplung.00239.2010.
22. Haine L, Bravais J, Yegen CH, et al. Sleep apnea in idiopathic pulmonary fibrosis: A molecular investigation in an experimental model of fibrosis and

intermittent hypoxia. Life (Basel Switzerland). 2021;11. https://doi.org/10.3390/life11090973.
23. Shi Z, Xu L, Xie H, et al. Attenuation of intermittent hypoxia-induced apoptosis and fibrosis in pulmonary tissues via suppression of ER stress activation. BMC Pulm Med. 2020;20:92. https://doi.org/10.1186/s12890-020-1123-0.
24. Newman AAC, Serbulea V, Baylis RA, et al. Multiple cell types contribute to the atherosclerotic lesion fibrous cap by PDGFRβ and bioenergetic mechanisms. Nat Metabolism. 2021;3:166–81. https://doi.org/10.1038/s42255-020-00338-8.
25. Orlich MM, Diéguez-Hurtado R, Muehlfriedel R, et al. Mural cell SRF controls pericyte Migration, vessel patterning and blood flow. Circul Res. 2022;131:308–27. https://doi.org/10.1161/circresaha.122.321109.
26. Caporarello N, Lee J, Pham TX, et al. Dysfunctional ERG signaling drives pulmonary vascular aging and persistent fibrosis. Nat Commun. 2022;13:4170. https://doi.org/10.1038/s41467-022-31890-4.
27. Labarca G, Vena D, Hu WH, et al. Sleep apnea physiological burdens and cardiovascular morbidity and mortality. Am J Respir Crit Care Med. 2023;208:802–13. https://doi.org/10.1164/rccm.202209-1808OC.
28. Myall KJ, West AG, Martinovic JL, et al. Nocturnal hypoxemia associates with symptom progression and mortality in patients with progressive fibrotic interstitial lung disease. Chest. 2023;164:1232–42. https://doi.org/10.1016/j.chest.2023.05.013.
29. Kalucka J, de Rooij LPMH, Goveia J et al. Single-Cell Transcriptome Atlas of Murine Endothelial Cells. *Cell* 180, 764–779.e720. https://doi.org/10.1016/j.cell.2020.01.015 (2020).
30. Wirka RC, Wagh D, Paik DT, et al. Atheroprotective roles of smooth muscle cell phenotypic modulation and the TCF21 disease gene as revealed by single-cell analysis. Nat Med. 2019;25:1280–9. https://doi.org/10.1038/s41591-019-0512-5.
31. Ding J, Fayyaz AI, Ding Y, Liang D, Luo M. Role of specificity protein 1 (SP1) in cardiovascular diseases: pathological mechanisms and therapeutic potentials. Biomolecules. 2024;14. https://doi.org/10.3390/biom14070807.
32. Pan H, Guo Z, Lv P, et al. Proline/serine-rich coiled-coil protein 1 inhibits macrophage inflammation and delays atherosclerotic progression by binding to Annexin A2. Clin Translational Med. 2023;13:e1220. https://doi.org/10.1002/ctm2.1220.
33. Verrecchia F, Rossert J, Mauviel A. Blocking sp1 transcription factor broadly inhibits extracellular matrix gene expression in vitro and in vivo: implications for the treatment of tissue fibrosis. J Invest Dermatol. 2001;116:755–63. https://doi.org/10.1046/j.1523-1747.2001.01326.x.
34. Xu Y, Zhang H, Chen Y, et al. SRF sumoylation modulates smooth muscle phenotypic switch and vascular remodeling. Nat Commun. 2024;15:6919. https://doi.org/10.1038/s41467-024-51350-5.
35. Gualdrini F, Esnault C, Horswell S, et al. SRF Co-factors control the balance between cell proliferation and contractility. Mol Cell. 2016;64:1048–61. https://doi.org/10.1016/j.molcel.2016.10.016.
36. Zhou N, Lee JJ, Stoll S, et al. Inhibition of SRF/myocardin reduces aortic stiffness by targeting vascular smooth muscle cell stiffening in hypertension. Cardiovascular Res. 2017;113:171–82. https://doi.org/10.1093/cvr/cvw222.
37. Murphy AM, Thomas A, Crinion SJ, et al. Intermittent hypoxia in obstructive sleep Apnoea mediates insulin resistance through adipose tissue inflammation. Eur Respir J. 2017;49. https://doi.org/10.1183/13993003.01731-2016.
38. Schaefer E, Wu W, Mark C, et al. Intermittent hypoxia is a Proinflammatory stimulus resulting in IL-6 expression and M1 macrophage polarization. Hepatol Commun. 2017;1:326–37. https://doi.org/10.1002/hep4.1045.
39. Wang Y, Lee MYK, Mak JCW, Ip MSM. Low-Frequency intermittent hypoxia suppresses subcutaneous adipogenesis and induces macrophage polarization in lean mice. Diabetes Metabolism J. 2019;43:659–74. https://doi.org/10.4093/dmj.2018.0196.
40. Liu J, Li T, Wu H, et al. Lactobacillus rhamnosus GG strain mitigated the development of obstructive sleep apnea-induced hypertension in a high salt diet via regulating TMAO level and CD4(+) T cell induced-type I inflammation. Biomed pharmacotherapy = Biomedecine Pharmacotherapie. 2019;112:108580. https://doi.org/10.1016/j.biopha.2019.01.041.
41. Qi P, Qi B, Ding Y, et al. Implications of obstructive sleep apnea in lung adenocarcinoma: A valuable omission in cancer prognosis and immunotherapy. Sleep Med. 2023;107:268–80. https://doi.org/10.1016/j.sleep.2023.05.013.
42. Cubillos-Zapata C, Avendaño-Ortiz J, Hernandez-Jimenez E, et al. Hypoxia-induced PD-L1/PD-1 crosstalk impairs T-cell function in sleep Apnoea. Eur Respir J. 2017;50. https://doi.org/10.1183/13993003.00833-2017.
43. Akbarpour M, Khalyfa A, Qiao Z, et al. Altered CD8 + T-Cell lymphocyte function and TC1 cell stemness contribute to enhanced malignant tumor properties in murine models of sleep apnea. Sleep. 2017;40. https://doi.org/10.1093/sleep/zsw040.
44. Chuang LP, Chen NH, Lin SW, et al. Increased C-C chemokine receptor 2 gene expression in monocytes of severe obstructive sleep apnea patients and under intermittent hypoxia. PLoS ONE. 2014;9:e113304. https://doi.org/10.1371/journal.pone.0113304.
45. Zhou J, Bai W, Liu Q, Cui J, Zhang W. Intermittent hypoxia enhances THP-1 monocyte adhesion and chemotaxis and promotes M1 macrophage polarization via RAGE. Biomed Res Int. 2018;2018(1650456). https://doi.org/10.1155/2018/1650456.

Publisher's Note

Springer Nature remains neutral with regard to jurisdictional claims in published maps and institutional affiliations.